The effect of soluble surfactant on the transient motion of a buoyancy-driven bubble

Savas Tasoglu, Utkan Demirci, and Metin Muradoglu

View Online   Export Citation

ARTICLES YOU MAY BE INTERESTED IN

The effect of soluble surfactant on the transient motion of a buoyancy-driven bubble

Savas Tasoglu,[1] Utkan Demirci,[2] and Metin Muradoglu[1]

[1]*Department of Mechanical Engineering, Koc University, Rumelifeneri Yolu, Sariyer 34450, Istanbul, Turkey*
[2]*Harvard-MIT Health Sciences and Technology, Harvard Medical School, Cambridge, Massachusetts 02115, USA*

The effect of soluble surfactants on the unsteady motion and deformation of a bubble rising in an otherwise quiescent liquid contained in an axisymmetric tube is computationally studied by using a finite-difference/front-tracking method. The unsteady incompressible flow equations are solved fully coupled with the evolution equations of bulk and interfacial surfactant concentrations. The surface tension is related to the interfacial surfactant concentration by a nonlinear equation of state. The nearly spherical, ellipsoidal, and dimpled ellipsoidal-cap regimes of bubble motion are examined. It is found that the surfactant generally reduces the terminal velocity of the bubble but this reduction is most pronounced in the nearly spherical regime in which the bubble behaves similar to a solid sphere and its terminal velocity approaches that of an equivalent solid sphere. Effects of the elasticity number and the bulk and interfacial Peclet numbers are examined in the spherical and ellipsoidal regimes. It is found that the surface flow and interfacial surfactant concentration profiles exhibit the formation of a stagnant cap at the trailing end of the bubble in the ellipsoidal regime at low elasticity and high interfacial Peclet numbers. Bubble deformation is first reduced due to rigidifying effect of the surfactant but is then amplified when the elasticity number exceeds a critical value due to overall reduction in the surface tension. © *2008 American Institute of Physics.*
[DOI: 10.1063/1.2912441]

I. INTRODUCTION

Surface active agents (surfactant) are either present as impurities that are difficult to remove from a system or they are deliberately added to fluid mixtures to manipulate interfacial flows. It has been well-known that the presence of surfactant in a fluid mixture can critically alter the motion and deformation of bubbles moving through a continuous liquid phase.[1,2] Probably, the best known example is the retardation effect of surfactant on the buoyancy-driven motion of small bubbles. Numerous experimental studies[1,3,4] have shown that the terminal velocity of a contaminated spherical bubble is significantly smaller than the classical Hadamard–Rybczynski prediction[5,6] and approaches the terminal velocity of an equivalent solid sphere. The physical mechanism for this behavior was first consistently explained by Frumkin and Levich[7] by noting that the surfactant adsorbed from the bulk fluid is convected toward the back of the bubble and the resulting Marangoni stresses act to reduce the interface mobility. This reduction in surface mobility increases the drag force and, thus, reduces the terminal velocity.[1,2,8]

The effect of surfactant on the rise of a single spherical bubble of various diameters has been experimentally studied by Bel Fdliha and Duineveld[9] and more recently by Zhang and Finch.[10] Bel Fdliha and Duineveld[9] measured the steady terminal rise velocity of bubble and reported a dependence on the bulk surfactant concentration. Zhang and Finch[10] measured the transient rise velocity of a spherical bubble for three different bulk surfactant concentrations. They showed that the distance to reach a steady-state gets shorter but the steady rise velocity remains the same as the bulk surfactant concentration increases. The motion of clean gas bubbles through capillaries with significant deformations and breakup has been studied by Borhan and Pallinti.[11,12] The effect of surfactant on the steady motion of a buoyancy-driven bubble moving through a capillary tube with significant deformations but without breakup was recently experimentally studied by Almatroushi and Borhan.[13] They found that the contamination retards the motion of small bubbles due to the development of adverse Marangoni stresses, whereas it enhances the mobility of large bubbles by increasing their deformability away from the tube wall. They also found that the steady rise velocity of small bubbles is unaffected, while the mobility of large bubbles is slightly increased as the bulk concentration is increased.

Due to complexity of the boundary conditions at deforming interface, the problem has been usually studied by using the simplifying assumptions of a nondeforming spherical bubble and the creeping flow limit. However, even in this limit, no complete analytical solution has been achieved. Frumkin and Levich[7] proposed a uniformly retarded interfacial velocity model that was also adopted by He *et al.*,[8] but this model has proved to be insufficient to fully explain experimental observations.[3,14] Savic[15] suggested the stagnant-cap model based on his own experimental observations. The stagnant-cap regime has been then extensively studied by several authors including Griffith,[16] Harper,[17–20] Davis and Acrivos,[21] Holbrook and Levan,[22,23] Sadhal and Johnson,[24] and He *et al.*[25] They all assumed creeping flow equations and

computed the drag force as a function of cap angle for a buoyancy-driven motion of a spherical bubble. In this regard, Harper[17–20] has made outstanding theoretical contributions to the problem and further studied diffusion boundary layer of surfactant around a stagnant-cap bubble, allowing both for adsorption and diffusion.[20] Bel Fdliha and Duineveld[9] extended the method developed by Sadhal and Johnson[24] to finite Reynolds numbers by solving the momentum equations around a spherical bubble with the stagnant-cap boundary conditions. Leppinen *et al.*[26,27] and McLaughlin[28] took a step forward and considered deforming interfaces but they both ignored the surfactant solubility. On the other hand, Cuenot *et al.*[29] considered the surfactant solubility but ignored bubble deformation and demonstrated the validity of stagnant-cap model to describe flow around a bubble slightly contaminated by a soluble surfactant. They also found that a simple relation between cap angle and bulk concentration cannot generally be obtained since diffusion from the bulk plays a significant role. Takemura[30] used a similar method to study the effects of Reynolds number and bulk surfactant concentration on the adsorption and the terminal velocity of a single bubble in an unbounded domain. They found that surfactant adsorption at the front of the bubble with respect to rise direction is lower than that at the back, and this difference increases with increasing Reynolds number and/or decreasing bulk surfactant concentration. Wang *et al.*[31] theoretically studied the slow motion of contaminated gas bubbles steadily rising in an unbounded liquid in creeping flow and showed that the mobility of surfactant-retarded bubble interface can be increased by raising the bulk surfactant concentration. Recently, Palaparthi *et al.*[32] theoretically and experimentally studied the effects of soluble surfactants on the motion of a spherical bubble in the stagnant-cap regime. They showed that very small bulk concentration can immobilize the entire bubble surface.

Full Navier–Stokes simulations with finite-rate mass exchange between the interface and bulk fluid have been recently performed by Sugiyama *et al.*,[33] Liao and McLaughlin,[34] and Li and Mao.[35] Sugiyama *et al.*[33] extended the study by Cuenot *et al.*[29] and allowed the bubble deformation. They solved the full Navier–Stokes equations coupled with an equation for the surfactant concentration on a body-fitted orthogonal grid and studied the effect of soluble surfactants on the motion of a deformable bubble in an unbounded domain. Liao and McLaughlin[34] studied the effects of soluble surfactant on unsteady motion of a single bubble rising in an unbounded water reservoir. They used a vorticity-stream function formulation with an adaptive body-fitted grid similar to the method developed by Ryskin and Leal.[36] They reported the time evolution of bubble rise velocity as a function of bulk surfactant concentration and surfactant solubility. Li and Mao[35] also used a body-fitted grid method and simulated the steady axisymmetrical motion of a single drop in an unbounded domain at moderate Reynolds numbers. They found that drag coefficient is significantly influenced by a minute amount of the surfactant, and the flow structure is sensitive to the bulk surfactant concentration. The common deficiencies of the previous full Navier–Stokes simulations can be summarized as follows:

(1) The wall effects are totally ignored and the bubble is assumed to be rising in an infinite domain. In many applications, the bubble moves through a finite size channel and channel walls have significant influence on motion and deformation of the bubble.[1,13]

(2) The terminal velocity of bubble is fixed throughout the simulation, which is impossible to experimentally achieve. Only exception is that Liao and McLaughlin[34] allowed the bubble to rise from rest but Liao *et al.*[37] reported significant numerical inaccuracies making their results unreliable.

The aim of the present paper is to remedy these deficiencies and investigate unsteady motion and deformation of a contaminated gas bubble rising in an otherwise quiescent liquid contained in an axisymmetrical capillary tube. For this purpose, the incompressible Navier–Stokes equations are solved fully coupled with the evolution equations of the interfacial and bulk surfactant concentrations by using a finite-difference/front-tracking method developed by Muradoglu and Tryggvason.[38] A nonlinear equation of state based on the Langmuir adsorption[39] is used to relate the surface tension coefficient to the interfacial surfactant concentration. A nearly spherical, ellipsoidal, and dimpled ellipsoidal-cap regimes are studied. The effect of tube wall on the terminal velocity of clean and contaminated bubble in the nearly spherical regime is investigated and the results are compared with the experimental correlations collected by Clift *et al.*[1] Extensive computations are performed to show the time evolution of interfacial and bulk surfactant concentrations, the effects of governing nondimensional numbers such as elasticity number, Peclet number based on bulk surfactant diffusivity, Peclet number based on interfacial surfactant diffusivity, Damkohler number, and Eötvös number on the terminal velocity and on the overall flow structure.

In the next section, the mathematical formulation is presented and the numerical method is briefly reviewed. The results are presented and discussed in Sec. III and conclusions are presented in Sec. IV.

II. FORMULATION AND NUMERICAL METHOD

The physical problem and computational domain are sketched in Fig. 1. The left boundary is the axis of symmetry and the flow is periodic in the axial direction. Here, the flow equations are described in the context of the finite-difference/front-tracking method. The fluid motion is assumed to be governed by the incompressible Navier–Stokes equations and we solve for the flow everywhere, both inside and outside of the bubble. By following Unverdi and Tryggvason,[40] a single set of governing equations can be written for the entire computational domain provided that the jumps in material properties such as density, viscosity, and molecular diffusion coefficient are correctly accounted for and surface tension is included.

In an axisymmetric coordinate system, the Navier–Stokes equations in conservative form are given by
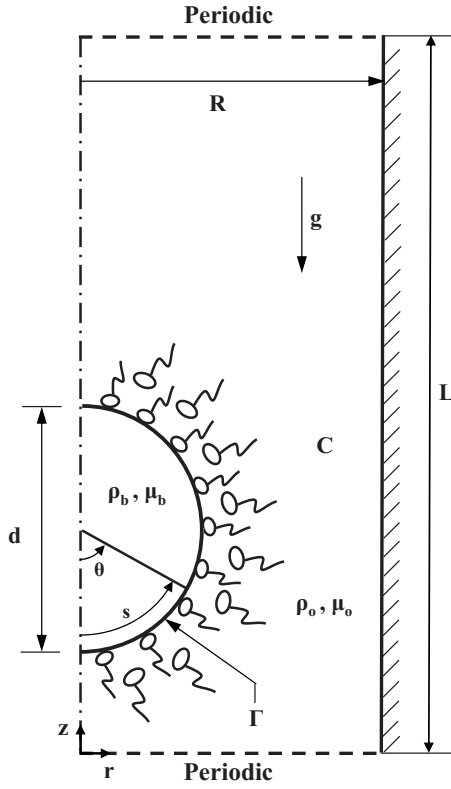
FIG. 1. Schematic illustration of the computational setup for a buoyancy-driven bubble rising in an axisymmetrical channel with soluble surfactant.

$$\frac{\partial \rho u}{\partial t} + \frac{1}{r}\frac{\partial r\rho u^2}{\partial r} + \frac{\partial \rho uv}{\partial z} = -\frac{\partial p}{\partial r} + \frac{\partial}{\partial r}\left(2\mu\frac{\partial u}{\partial r}\right) + 2\mu\frac{\partial}{\partial r}\left(\frac{u}{r}\right)$$
$$+ \frac{\partial}{\partial z}\mu\left(\frac{\partial v}{\partial r} + \frac{\partial u}{\partial z}\right)$$
$$- \int_A \sigma(\Gamma)\kappa\mathbf{n}\,\delta(\mathbf{x}-\mathbf{x}_f)dA\cdot\hat{\mathbf{i}}_r,$$

$$\frac{\partial \rho v}{\partial t} + \frac{1}{r}\frac{\partial r\rho uv}{\partial r} + \frac{\partial \rho v^2}{\partial z} = -\frac{\partial p}{\partial z} + \frac{\partial}{\partial r}\mu r\left(\frac{\partial v}{\partial r} + \frac{\partial u}{\partial z}\right)$$
$$+ \frac{\partial}{\partial z}\left(2\mu\frac{\partial v}{\partial z}\right) + (\rho-\bar{\rho})g$$
$$- \int_A \sigma(\Gamma)\kappa\mathbf{n}\,\delta(\mathbf{x}-\mathbf{x}_f)dA\cdot\hat{\mathbf{i}}_z,$$

(1)

where u and v are the velocity components in the radial and axial directions, respectively, p is the pressure, g is the gravitational acceleration, and ρ and μ are the discontinuous density and viscosity fields, respectively. The effects of surface tension is included as a body force in the last term on the right hand side, where σ is the surface tension that is a function of the surfactant concentration Γ at the interface, κ is twice the mean curvature, and $\mathbf{n}$ is a unit vector normal to the interface. The surface tension only acts on the interface as indicated by the three-dimensional delta function δ, whose arguments $\mathbf{x}$ and $\mathbf{x}_f$ are the point at which the equation is evaluated and the point at the interface, respectively. By following Jan[41] and Muradoglu and Tryggvason,[38] the buoy-

ancy force is added to the right hand side of the momentum equation in the form $(\rho-\bar{\rho})g$, where $\bar{\rho}$ is the average density of the whole computational domain. Note that the extra term $\bar{\rho}g$ in Eq. (1) is a hydrostatic force added to keep the net vertical momentum constant.[41]

The Navier–Stokes equations are supplemented by the incompressibility condition,

$$\frac{1}{r}\frac{\partial ru}{\partial r} + \frac{\partial v}{\partial z} = 0. \tag{2}$$

We also assume that the material properties remain to be constant following a fluid particle, i.e., $D\rho/Dt=0$ and $D\mu/Dt=0$, where D/Dt is the material derivative. The density and viscosity discontinuously vary across the fluid interface and are given by

$$\rho = \rho_b I(r,z,t) + \rho_o[1 - I(r,z,t)],$$
$$\mu = \mu_b I(r,z,t) + \mu_o[1 - I(r,z,t)], \tag{3}$$

where the subscripts b and o denote properties of the bubble and the ambient fluids, respectively, and $I(r,z,t)$ is the indicator function defined as

$$I(r,z,t) = \begin{cases} 1 & \text{in bubble fluid,} \\ 0 & \text{in bulk fluid.} \end{cases} \tag{4}$$

Concentration of surfactant on the interface Γ is defined as

$$\Gamma = \frac{M_s}{A}, \tag{5}$$

where M_s is the adsorbed mass of surfactant and A is the surface area. Surface tension decreases proportional to the surfactant concentration at the interface according to the equation of state derived from Langmuir adsorption,[39]

$$\sigma = \sigma_s + \mathcal{R}T\Gamma_\infty \ln\left(1 - \frac{\Gamma}{\Gamma_\infty}\right), \tag{6}$$

where $\mathcal{R}$ is the ideal gas constant, T is the absolute temperature, σ_s is the surface tension of clean interface, and Γ_∞ is the maximum packing concentration. Equation (6) can also be written as

$$\sigma = \sigma_s\left[1 + \beta_s \ln\left(1 - \frac{\Gamma}{\Gamma_\infty}\right)\right], \tag{7}$$

where $\beta_s = \mathcal{R}T\Gamma_\infty/\sigma_s$ is the *elasticity* number. The physico-chemical parameter β_s is a measure of the sensitivity of interfacial tension to variations in surfactant concentration. Equation (7) is slightly modified to avoid negative values of the surface tension as

$$\sigma = \sigma_s\left\{\max\left[\epsilon_\sigma, 1 + \beta_s \ln\left(1 - \frac{\Gamma}{\Gamma_\infty}\right)\right]\right\}, \tag{8}$$

where ϵ_σ is taken as 0.05 in the present study. The surfactant concentration Γ evolves by[42]

$$\frac{\partial \Gamma}{\partial t} + \nabla_s\cdot(\Gamma\mathbf{U}_s) = D_s\nabla_s^2\Gamma + \dot{S}_\Gamma, \tag{9}$$

where the gradient operator along the interface is defined as

$$\nabla_s = \nabla - \mathbf{n}(\mathbf{n} \cdot \nabla). \tag{10}$$

In Eq. (9), $\mathbf{U}_s$ is the tangential velocity on the interface, D_s is the diffusion coefficient along the interface, and $\dot{S}_\Gamma$ is the source term given by

$$\dot{S}_\Gamma = k_a C_s(\Gamma_\infty - \Gamma) - k_b \Gamma, \tag{11}$$

where k_a and k_b are adsorption and desorption coefficients, respectively, and C_s is the surfactant concentration in fluid immediately adjacent to the interface. The bulk surfactant concentration C is governed by the advection-diffusion equation

$$\frac{\partial C}{\partial t} + \nabla \cdot (C\mathbf{u}) = \nabla \cdot (D_{co} \nabla C), \tag{12}$$

where the coefficient D_{co} is related to the molecular diffusion coefficient D_c and the indicator function I as

$$D_{co} = D_c[1 - I(r,z,t)]. \tag{13}$$

The source term in Eq. (9) is related to the bulk concentration as[43]

$$\dot{S}_\Gamma = -D_{co}(\mathbf{n} \cdot \nabla C|_{\text{interface}}). \tag{14}$$

By following Muradoglu and Tryggvason,[38] the boundary condition at the interface given by Eq. (14) is first converted into a source term in a conservative manner by assuming that all the mass transfer between the interface and the bulk takes place in a thin *adsorption* layer adjacent to the interface. In this method, total amount of mass adsorbed on the interface is distributed over the adsorption layer and added to the bulk concentration evolution equation as a negative source term in a conservative manner. Equation (12) thus becomes

$$\frac{\partial C}{\partial t} + \nabla \cdot (C\mathbf{u}) = \nabla \cdot (D_{co} \nabla C) + \dot{S}_C, \tag{15}$$

where $\dot{S}_C$ is the source term evaluated at the interface and distributed onto the adsorption layer in a conservative manner. With this formulation, all the mass of the bulk surfactant to be adsorbed by the interface has been already consumed in the adsorption layer before the interface. Hence, the boundary condition at the interface simplifies to be $\mathbf{n} \cdot \nabla C|_{\text{interface}} = 0$.

The flow equations [(Eqs. (1) and (2))] are solved fully coupled with the evolution equations for interfacial concentration [Eq. (9)] and for bulk concentration [Eq. (15)] by the finite-difference/front-tracking method.[38] The momentum and the continuity equations are discretized by using a first-order time integration method and a second-order centered difference approximation for the spatial derivatives. The discretized equations are solved on a stationary, staggered Eulerian grid by using the marker-and-cell method.[44] The bulk surfactant concentration is stored at the same location as the pressure on the staggered grid. The evolution equation for the bulk surfactant concentration is solved fully coupled with the flow equations by using second-order centered differences for the spatial derivatives and a first-order Euler method for the time integration. No-slip and no-flux boundary conditions are applied at the tube wall, while the symmetry and periodic boundary conditions are used at the tube centerline and in the axial direction, respectively.

A separate Lagrangian grid is used to track the bubble-ambient fluid interface. The Lagrangian grid consists of linked marker points (the front) that move with the local flow velocity that is interpolated from the stationary Eulerian grid. The piece of the Lagrangian grid between two marker points is called a front element. The interfacial surfactant concentration equation (9) is solved on the Lagrangian grid by using second-order centered differences for the spatial derivatives and a first-order Euler method for the time integration. The Lagrangian grid is also used to find the surface tension, which is then distributed onto Eulerian grid points near the interface by using Peskin's cosine distribution function,[45] and added to the momentum equations as body forces as described by Tryggvason et al.[46]

An indicator function is defined such that it is unity inside the bubble and zero outside. At each time step, the indicator function is computed and is used to set the fluid properties inside and outside the bubble. To do this, unit magnitude jumps are distributed in a conservative manner on the Eulerian grid points near the interface by using Peskin's cosine distribution function[45] and are then integrated to compute the indicator function everywhere. The computation of the indicator function requires solution of a separable Poisson equation and yields a smooth transition of the indicator function across the interface. Then, the fluid properties are set as a function of the indicator function. The indicator function is also used to distribute the surfactant source term outside of the bubble.[38]

The Lagrangian grid is restructured at every time step by deleting the front elements that are smaller than a prespecified lower limit and by splitting the front elements that are larger than a prespecified upper limit in the same way as described by Tryggvason et al.[46] to keep the front element size nearly uniform and comparable to the Eulerian grid size. Restructuring the Lagrangian grid is crucial since it avoids unresolved wiggles due to small elements and lack of resolution due to large elements. Note that restructuring the Lagrangian grid is performed such that the mass conservation is strictly satisfied for the surfactant at the interface. The details of the front-tracking method can be found in the works of Unverdi and Tryggvason[40] and Tryggvason et al.[46] For a complete description of the finite-difference/front-tracking method for the interfacial flows with soluble surfactants, refer to the work of Muradoglu and Tryggvason.[38]

The governing equations are solved in their dimensional forms, and the results are expressed in terms of relevant nondimensional quantities. Let $\mathcal{L}$ and $\mathcal{U}$ be appropriately defined length and velocity scales, respectively, and $\mathcal{T} = \mathcal{L}/\mathcal{U}$ be the time scale, then governing nondimensional numbers can be summarized as
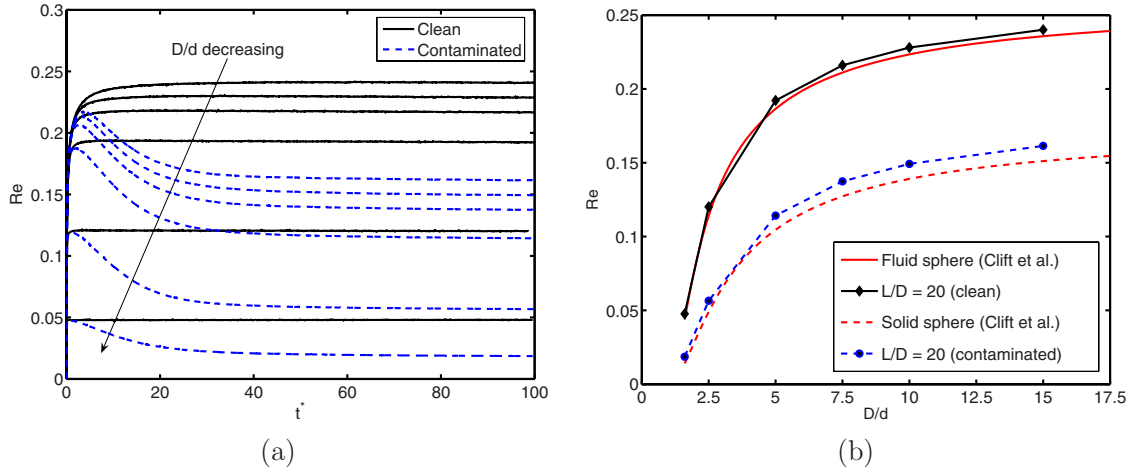
FIG. 2. (Color online) Spherical bubble. (a) Reynolds number vs nondimensional time for $D/d=1.6, 2.5, 5, 7.5, 10,$ and 15, and (b) steady Reynolds number vs nondimensional channel diameter for clean (solid lines) and contaminated (dashed lines) bubbles. (Eo=1 and Mo=0.1.)

$$\mathrm{Re}=\frac{\rho_o \mathcal{U}L}{\mu_o}, \quad \mathrm{Pe}_c=\frac{\mathcal{U}L}{D_c}, \quad \mathrm{Pe}_s=\frac{\mathcal{U}L}{D_s}, \quad \frac{\rho_b}{\rho_o}, \quad \frac{\mu_b}{\mu_o},$$

$$k=\frac{k_a C_\infty}{k_b}, \quad \mathrm{Bi}=\frac{k_b \mathcal{L}}{\mathcal{U}}, \quad \mathrm{Da}=\frac{\Gamma_\infty}{\mathcal{L} C_\infty}, \quad \beta_s=\frac{\mathcal{R}T\Gamma_\infty}{\sigma_s}, \tag{16}$$

where Re, Pe_c, Pe_s, k, Bi, Da, and β_s are the Reynolds number, the Peclet number based on bulk surfactant diffusivity, the Peclet number based on interface surfactant diffusivity, the dimensionless adsorption depth, the Biot number, the Damkohler number, and the elasticity number, respectively. Note that Pe_c and Pe_s are referred as the bulk and interfacial Peclet numbers, respectively.

III. RESULTS AND DISCUSSION

We consider a straight cylindrical capillary tube of radius R and assume that the flow is axisymmetric. The physical problem and computational setup are sketched in Fig. 1. The computational domains are R in radial direction and L in the axial direction. Periodic boundary conditions are applied in the axial direction. Symmetry and no-slip boundary conditions are utilized at the centerline and at the wall of the tube, respectively. The bubble is initially located at the channel centerline close to the south boundary. The interface is initially clean and the surfactant concentration is uniform in the bulk fluid at $C=C_\infty$. The bubble rises in the tube solely due to density difference between the bubble and the ambient fluids.

Besides the nondimensional numbers given by Eq. (16), there are four additional independent parameters for this problem: The Eötvös number $\mathrm{Eo}=\Delta\rho g d^2/\sigma_s$, the Morton number $\mathrm{Mo}=\Delta\rho g \mu_o^4/\rho_o^2\sigma^3$, the nondimensional channel diameter D/d, and the nondimensional channel length L/d. The length and velocity scales are taken as $\mathcal{L}=d/2$ and $\mathcal{U}=V_{\mathrm{HR}}$, respectively, where V_{HR} is the terminal velocity given by Hadamard–Rybczynski solution[1] for a spherical bubble moving in an infinite domain, i.e.,

$$V_{\mathrm{HR}}=\frac{2}{3}\frac{ga^2\Delta\rho}{\mu_o}\frac{\mu_o+\mu_b}{2\mu_o+3\mu_b}, \tag{17}$$

where a is the bubble radius. The time scale is then defined as $\mathcal{T}=\mathcal{L}/\mathcal{U}$. The parameters Pe_c, Pe_s, Bi, and Da are defined based on these scales. However, nondimensional time (t^*) and Reynolds number (Re) are defined by using the actual bubble terminal velocity (V_b) as the velocity scale and $\sqrt{d/g}$ as the time scale to facilitate direct comparison of the computational results with the available experimental data.

First, we study the effects of surfactant on the terminal velocity of a nearly spherical bubble slowly moving in an axisymmetrical channel of various diameters. For this purpose, computations are performed for clean and contaminated bubbles moving in a channel with the diameters ranging between $D=1.6d$ and $15d$. Computations are performed by keeping the nondimensional parameters constant at $L/d=20$, $\rho_b/\rho_o=0.1$, $\mu_b/\mu_o=0.025$, $\mathrm{Pe}_c=10$, $\mathrm{Pe}_s=100$, $k=1$, $\mathrm{Da}=10$, $\mathrm{Bi}=20$, and $\beta_s=0.5$. The Eötvös and Morton numbers are chosen as $\mathrm{Eo}=1$ and $\mathrm{Mo}=0.1$ for which a clean bubble moves slowly with a nearly spherical shape. The steady Reynolds number based on the bubble terminal velocity in an unbounded domain is 0.26, which is well within the validity of the experimental correlations collected by Clift et al.[1] for clean and contaminated bubbles. Note that this case is referred as "spherical bubble" in this paper.

The grid convergence of the present finite-difference/front-tracking method has been examined,[38] and it was demonstrated that it is sufficient to resolve the bubble with about 40 grid points in the axial direction to reduce the spatial error below 5% for such problems. Therefore, a similar grid convergence study is not repeated here and computational grids are selected such that the bubble is resolved by about 40 grid points in the axial direction in all results presented in this paper unless specified otherwise.

The Reynolds number is plotted in Fig. 2(a) as a function of nondimensional time for the clean and contaminated bubbles moving in a channel with $D/d=1.6, 2.5, 5.0, 7.5, 10.0,$ and 15.0. The retardation effect of the surfactant is
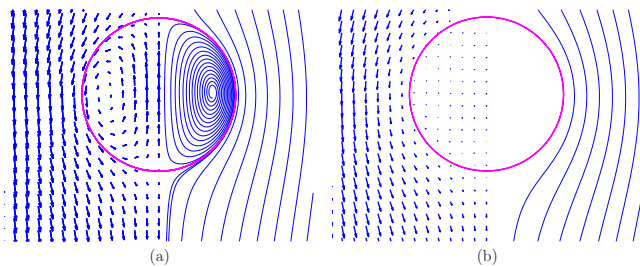
FIG. 3. (Color online) Spherical bubble. The streamlines and the velocity vectors at steady-state in a coordinate system moving with the bubble centroid for (a) a clean bubble and (b) a contaminated bubble. Every third grid points are used in the velocity vector plots. (Eo=1 and Mo=0.1.)

clearly seen in this figure; i.e., in the clean case, the bubble continuously accelerates and reaches a steady Reynolds number (or terminal velocity), while in the contaminated case, the bubble first accelerates, reaches a peak velocity but then decelerates as the surfactant accumulates at the interface, and finally reaches a steady Reynolds number. The computed steady Reynolds number is plotted in Fig. 2(b) as a function of the channel confinement (D/d) and compared to the available experimental data collected by Clift *et al.*[1] both for the clean and contaminated cases. Note that, in the contaminated bubble case, the computational results are compared to the experimental correlation obtained for an equivalent solid sphere to show the rigidifying effect of the surfactant. The computational results are shown by connected symbols, while the experimental data are shown by solid and dashed lines for the fluid and solid spheres, respectively. As seen in Fig. 2, there is good agreement between the computational and experimental results for the clean bubble case, and the steady Reynolds number of the contaminated bubble approaches that of an equivalent solid sphere. The small discrepancy between the computed and experimental results for the clean bubble is partly attributed to the finite length of the periodic channel, and the difference decreases as the channel length increases as discussed by Muradoglu and Tryggvason.[38] The flow fields are plotted in Fig. 3 both for the clean and contaminated bubbles rising in a large

channel with $D=15d$ and $L=20d$ when bubbles reach a steady motion. A big vortex is created inside the clean bubble, while the vortex inside the contaminated bubble nearly vanishes as it reaches a steady motion, as depicted in Fig. 3(b). This visually indicates the immobilization of the interface by the surfactant. The streamline patterns also change as the bubble gets contaminated. The spacing between streamlines is smaller when the bubble is clean and becomes larger as the bubble gets contaminated. The immobilizing effect of surfactant can be better seen from the surface velocities of the clean and contaminated bubbles plotted in Fig. 4(a). In this figure, the nondimensional surface velocities are plotted as a function of nondimensional arc length measured from the centerline in the counterclockwise direction for the nondimensional channel diameters of D/d =1.6, 2.5, 5.0, and 15.0 at $t^*=100$. Figure 4(a) clearly shows that the nondimensional steady surface velocity nearly vanishes for the contaminated bubble case. On the other hand, the clean bubble surface has a significant velocity and it decreases while D/d ratio decreases due to the increased wall effect. The wall effect is also apparent in distribution of interfacial surfactant concentration, as seen in Fig. 4(b), where variation of interfacial surfactant concentration is plotted as a function of non-dimensional arc length. The wall has a considerable effect on the interfacial surfactant concentration when $D/d \leq 2.5$, and the wall effect quickly reduces and becomes negligible when $D/d \geq 5$.

Computations are performed to examine the effect of the elasticity number on the motion of a spherical bubble rising in a channel with $D=5d$. For this purpose, the elasticity number is varied between $\beta_s=0$ and 1 and $Pe_c=1000$, while the other parameters are kept the same. Figure 5 shows the bubble interface together with the contour plots of the constant surfactant concentration in the bulk fluid and the surfactant concentration distribution along the interface for β_s =0.1 and 1 at $t^*=103.1$. The interfacial surfactant concentration becomes smoother as β_s increases mainly due to reduced mobility of interface for larger values of β_s. Conversely, as β_s decreases, the interface mobility increases so that the surfactant adsorbed at the leading edge of the bubble
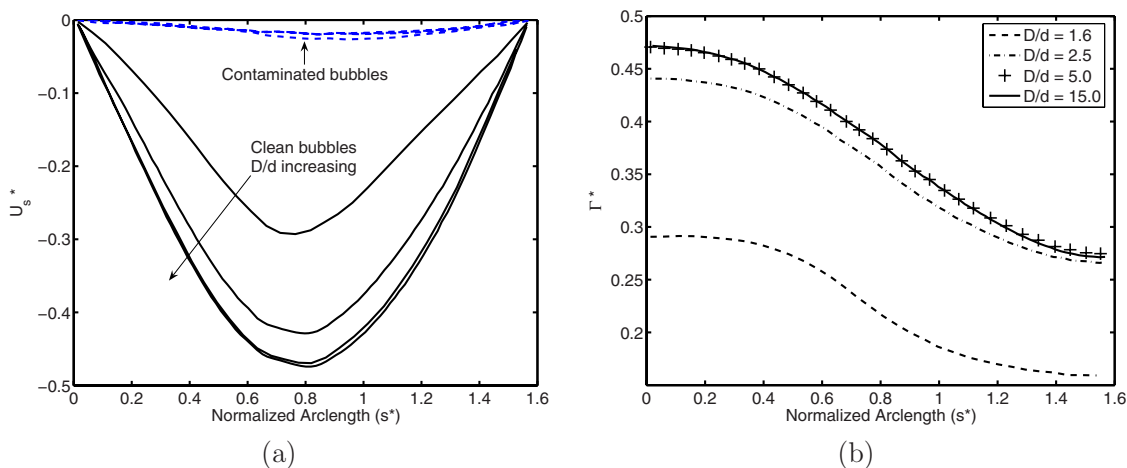

FIG. 4. (Color online) Spherical bubble. (a) Surface velocity profiles of a clean (solid lines) and a contaminated (dashed lines) bubble, and (b) the interfacial surfactant concentration profiles for the channel diameters D/d=1.6, 2.5, 5, and 15 at $t^*=100$. (Eo=1 and Mo=0.1.)
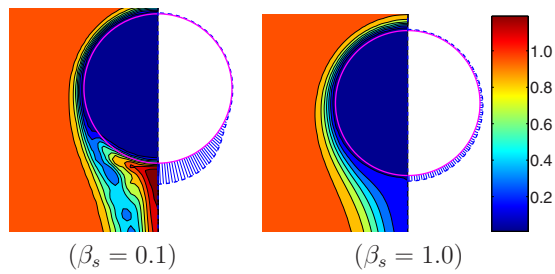
FIG. 5. (Color online) Spherical bubble. The contour plots of constant surfactant concentration in the bulk fluid (left side) and the distribution of the surfactant concentration at the interface (right side) with β_s=0.1 (left plot) and 1 (right plot) at t^*=103.1. Contour levels are the same in both cases. (Pe$_c$=1000, Eo=1, and Mo=0.1.)
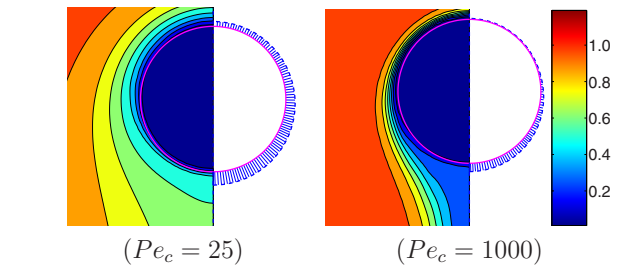

FIG. 7. (Color online) Spherical bubble. The contour plots of constant surfactant concentration in the bulk fluid (left side) and the distribution of the surfactant concentration at the interface (right side) with Pe$_c$=25 (left plot) and 1000 (right plot) at t^*=103.1. Contour levels are the same in both cases. (β_s=0.5, Eo=1, and Mo=0.1.)

is quickly convected along the interface resulting in accumulation of surfactant at the back of the bubble. The effects of β_s on the interface mobility and on the interfacial surfactant concentration distribution can be better seen in Fig. 6, where the nondimensional surface velocity and interfacial surfactant concentration are plotted as a function of nondimensional arc length for β_s=0.1, 0.5, and 1 at t^*=103.1. Here, as β_s increases, interfacial surfactant concentration becomes more uniform and the magnitude of the surface velocity significantly decreases.

For the spherical bubble case, we now examine the effect of the bulk Peclet number (Pe$_c$). For this purpose, Pe$_c$ is varied while the elasticity number is kept constant at β_s =0.5. The contour plots of the constant bulk surfactant concentration and the surfactant concentration distribution at the interface are plotted in Fig. 7 for Pe$_c$=25 and 1000 at t^* =103.1. As shown in this figure, the surfactant concentration at the interface increases as Pe$_c$ decreases due to enhanced diffusivity of the surfactant in the ambient fluid. A thin boundary layer created on the bubble surface can also be seen from the contour levels of the bulk concentration for Pe$_c$=1000. Figure 8 shows the variation of nondimensional surface velocity and interfacial surfactant concentration as a function of nondimensional arc length for Pe$_c$=25, 100, 500, and 1000 at t^*=103.1. It is clearly seen that, as Pe$_c$ de-

creases, the magnitude of the nondimensional surface velocity diminishes while the interfacial surfactant concentration increases.

In the experiment, the bulk surfactant concentration is usually varied while the other parameters are kept constant. To mimic this, the Damkohler number is varied while keeping the other parameters the same as in Fig. 4 for a bubble rising in the channel with D=5d and L=20d. In Fig. 9, the Reynolds number is plotted for various values of Damkohler number ranging between Da=1.25 and 10. As can be seen in this figure, the distance to reach a steady-state gets shorter as Da decreases but the steady rise velocity seems to be independent of Da. This is qualitatively in a good agreement with the experimental observations of Zhang and Finch.[10]

Next, we investigate the effect of the soluble surfactants on the motion of a single bubble with significant deformation. We set Eo=10 and Mo=0.001 for which a clean bubble has an ellipsoidal shape in an unbounded domain as discussed by Clift *et al.*[1] For this case, the channel size is L =50d in the axial direction and D=5d in the radial direction, and it is resolved by a 96×1920 uniform grid. The parameters are kept constant at ρ_b/ρ_o=0.1, μ_b/μ_o=0.025, k=1, Da=10, and Bi=0.75. First, effect of the elasticity number is examined. For this purpose, computations are performed for β_s=0, 0.1, 0.25, 0.5, and 1 while keeping Pe$_c$=1000 and
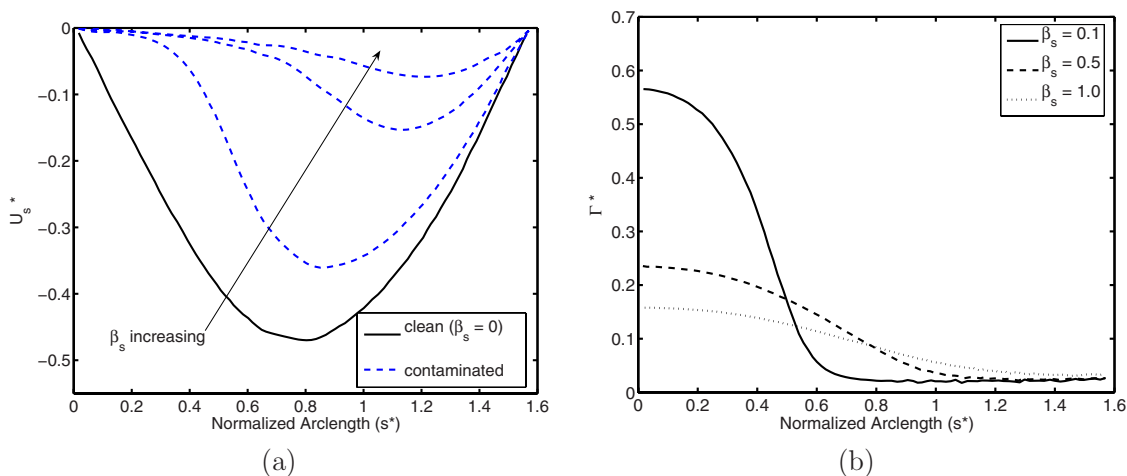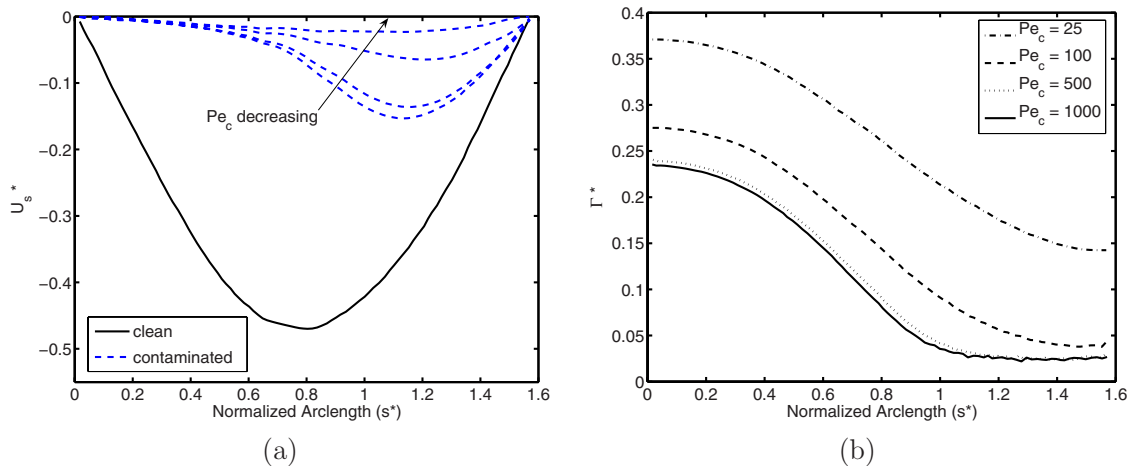

FIG. 6. (Color online) Spherical bubble. (a) The surface velocity and (b) interfacial surfactant concentration as a function of arc length measured from the centerline in the counterclockwise direction for β_s=0.1, 0.5, and 1 at t^*=103.1.

FIG. 8. (Color online) Spherical bubble. (a) The surface velocity and (b) interfacial surfactant concentration as a function of arc length measured from the centerline in the counterclockwise direction for Pe_c=25, 100, 500, and 1000 at t^*=103.1. (Eo=1 and Mo=0.1.)

Pe_s=100. Figure 10 illustrates the variation of Reynolds number as a function of the nondimensional time for various elasticity values. As seen in this figure, terminal velocity decreases with increasing elasticity number but the reduction in the terminal velocity is not as dramatic as that observed in the spherical regime. Note that the computed Reynolds number of the clean bubble is 23.8 which is in good agreement with the experimental value of 23.3, see for instance, the work of Clift et al.[1] The time evolutions of the surface velocity and interfacial surfactant concentration are plotted in Figs. 11(a) and 11(b), respectively, for β_s=0.1 and β_s=1. The results are taken at t^*=9.7, 28.4, 48.4, and 67.8. It is seen in Fig. 11(a) that the surface velocity does not significantly change in the case of β_s=0.1, while its amplitude quickly decreases and the interface becomes nearly immobile in the case of β_s=1 as bubble approaches a steady motion. The elasticity number also influences the interfacial surfactant distribution, as seen in Fig. 11(b). In the case of small elasticity number (β_s=0.1), the surfactant adsorbed at the leading edge of the bubble is quickly swept along the interface and accumulated at the back of the bubble due to the large surface mobility. The surfactant concentration is nearly

flat at the back of the bubble and rapidly decreases at about s^*=0.6, which is consistent with the stagnant-cap theory.[1] However, there is no discontinuity in the interfacial surfactant concentration partly due to diffusion along the interface and partly due to the Marangoni stresses acting in the opposite direction of the flow shear stress. In the case of large elasticity number (β_s=1), the surfactant concentration is still flat at the back and it decreases at the front of the bubble. However, the distribution is more uniform and the transition is much smoother than that in the case of β_s=0.1. The elasticity number also has a significant influence on the bubble deformation and on the overall flow structure, as shown in Fig. 12, where the contours of constant bulk surfactant concentration are plotted together with the surfactant distribution at the interface in the top row, and the velocity vectors and streamlines are plotted in the vicinity of the bubble with respect to a coordinate system moving with the bubble centroid in the bottom row for β_s=0.1, 0.25, 0.5, and 1. As seen, the surfactant adsorbed by the interface is swept back by the oncoming flow and accumulated there for all cases. However, the interfacial surfactant distribution gets to be more uniform as the elasticity number increases due to enhanced
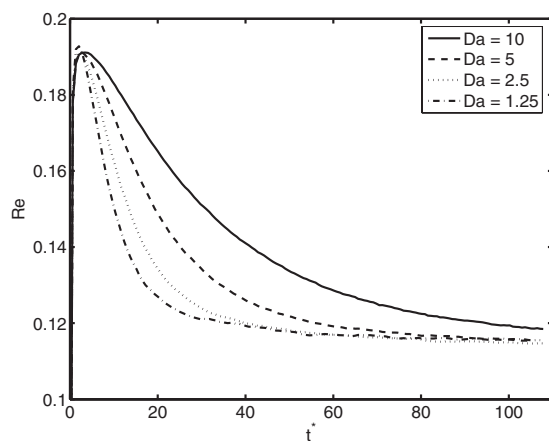

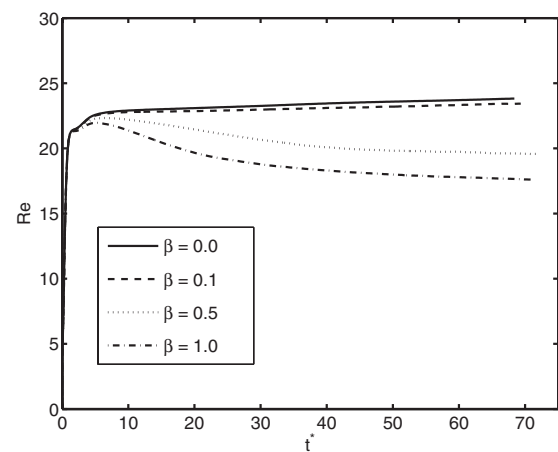FIG. 9. Spherical bubble. Reynolds number vs time for Da=10, 5, 2.5, and 1.25. (Eo=1 and Mo=0.1.)

FIG. 10. Ellipsoidal bubble. Reynolds number vs time for β_s=0.0, 0.1, 0.5, and 1.0. (Eo=10 and Mo=0.001.)
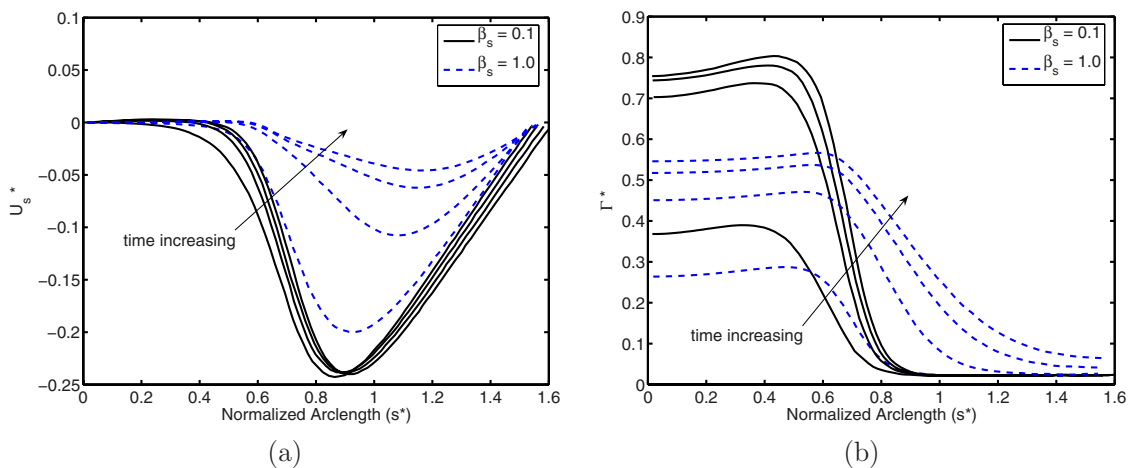
FIG. 11. (Color online) Ellipsoidal bubble. (a) Surface velocity and (b) interfacial surfactant concentration vs arc length measured from the centerline in the counter-clockwise direction for $\beta_s=0.1$ (solid lines) and 1.0 (dashed lines) at times $t^*=9.7$, 28.4, 48.4, and 67.8. (Eo=10 and Mo=0.001.)

immobilizing effect of the surfactant at large β_s. As the surfactant is convected back along the interface and is accumulated at the back of the bubble, its concentration continuously increases and eventually exceeds the equilibrium interfacial concentration of the interface. After that, the excessive surfactant is released into the bulk fluid and the interfacial surfactant concentration eventually becomes steady. This can be clearly seen from the contour plots of the bulk surfactant concentration in the top row of Fig. 12 and the time evolution of the interfacial surfactant concentration in Fig. 11(b) especially for the cases of small elasticity numbers, i.e., $\beta_s \leq 0.5$. The surfactant is mainly released from the interface into the bulk fluid near the stagnation points (e.g., at about $s^*=0.6$ for this case), making the surfactant concentration relatively high in the bulk fluid there. The elasticity number also has a significant influence on the overall flow structure, as seen in the velocity vectors and streamline plots in the bottom row of Fig. 12. For instance, while there is a big vortex created inside and a small recirculation region at the back of the bubble for small elasticity numbers (e.g.,

$\beta_s=0.1$), the big vortex is broken into two smaller vortices and the recirculation region gets larger as the elasticity number is increased. It is also interesting to observe that, as the elasticity number increases, the bubble deformation first decreases due to rigidifying effect of the surfactants but it then increases due to overall reduction in surface tension. This can be better seen in Fig. 13, where the bubble deformation is plotted as a function of time for various values of β_s. Note that the deformation is defined as

$$\text{deformation} = \frac{W_b - H_b}{W_b + H_b}, \qquad (18)$$

where W_b and H_b are the maximum bubble dimensions in the radial and axial directions, respectively. As can be seen in Figs. 12 and 13, bubble deformation is larger in the case of $\beta_s=0.1$ than in $\beta_s=0.5$ case but smaller than in $\beta_s=1$ case. The surface velocity and the interfacial surfactant distribution are plotted in Figs. 14(a) and 14(b), respectively, as a
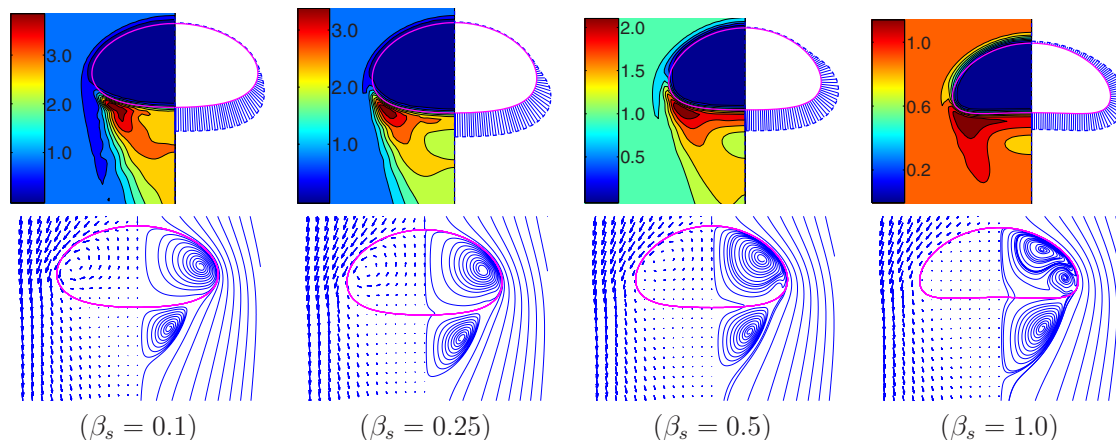

FIG. 12. (Color online) Ellipsoidal bubble. (Top row) The contour plots of the constant surfactant concentration in the bulk fluid (left side) and the distribution of the surfactant concentration at the interface (right side) with (from left to right) $\beta_s=0.1$, 0.25, 0.5, and 1.0. (Bottom row) The streamlines and the velocity vectors in a coordinate system moving with the bubble centroid. Every third grid point is used in the vector plots. (Eo=10, Mo=0.001, Pe$_c$=1000, Pe$_s$ =100, and $t^*=67.8$.)
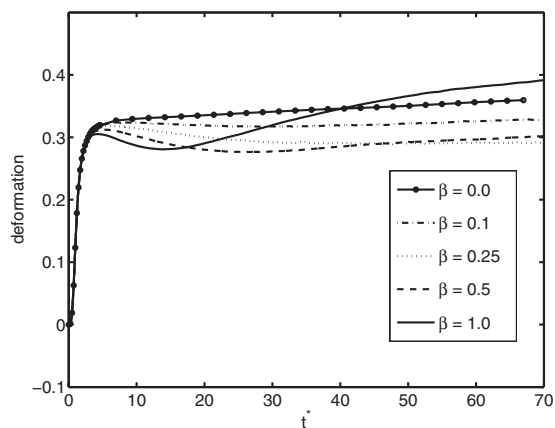
FIG. 13. Ellipsoidal bubble. Effect of elasticity number on bubble deformation. (Eo=10, Mo=0.001, Pe$_c$=1000, and Pe$_s$=100.)

function of the arc length for various values of β_s. Similar to the spherical case, the surface mobility significantly reduces and the surfactant distribution becomes more uniform along the interface as β_s increases.

The effect of the bulk Peclet number is also examined for the ellipsoidal regime. For this purpose, computations are performed for Pe$_c$=25, 100, 500, and 1000 while keeping Pe$_s$ and β_s fixed at 100 and 0.5, respectively. The time evolution of the surface velocity and distribution of the interfacial surfactant concentration are plotted in Figs. 15(a) and 15(b), respectively, for Pe$_c$=25 and 1000 cases. It can be seen from these figures that both the surface velocity and interfacial surfactant concentration reach steady state faster for Pe$_c$=25 than for Pe$_c$=1000 due to enhanced surfactant diffusion from bulk fluid to the bubble surface for small Pe$_c$. The constant contours of the bulk surfactant concentration and the interfacial surfactant concentration distributions are plotted in the top row of Fig. 16 at t^*=67.8, while the velocity vectors and streamlines in the vicinity of the bubble are shown in the bottom row. We observe that Pe$_c$ does not have a big effect on the interfacial surfactant distribution and overall flow structure in the range between Pe$_c$=25 and 1000.

This can also be seen in the surface velocity and interfacial surfactant distribution plotted in Fig. 17. However it has stronger effect on the bulk surfactant concentration as the surfactant released from the interface near the stagnation point is quickly dissipated by the molecular diffusion, making the bulk surfactant concentration more homogeneous in the recirculation region at the back of the bubble as Pe$_c$ gets smaller. In addition, the bulk surfactant concentration boundary layer at the leading edge of the bubble gets thinner as Pe$_c$ increases, as can be seen from the contour plots in the top row of Fig. 16.

Finally, the effects of the interfacial Peclet number (Pe$_s$) are investigated for the ellipsoidal case by varying Pe$_s$ from 100 to 10^4 while keeping Pe$_c$ and β_s fixed at 1000 and 0.5, respectively. The contours of the constant bulk surfactant concentration and the distribution of the interfacial surfactant concentration are plotted in the top row of Fig. 18, while the velocity vectors and streamlines are depicted in the bottom row for various values of Pe$_s$. Figure 18 shows that Pe$_s$ generally has a significant influence on the bubble dynamics. The interface surfactant concentration becomes more uniform as Pe$_s$ decreases since surface diffusion counteracts the convection of the surfactant by the surface velocity. At high values of Pe$_s$, the surface diffusion becomes weak and the interfacial surfactant distribution approaches the stagnant-cap regime. In this regime, large concentration gradient induces large Marangoni stresses especially near the stagnation point and, thus, reduces the mobility of the interface. Similar to the large elasticity number cases, the big vortex inside the bubble is broken to create a smaller vortex after a critical value of Pe$_s$, i.e., about Pe$_s$=100 in this case, and the smaller vortex gets larger when Pe$_s$ is increased beyond the critical value. In addition, the recirculation zone behind the bubble gets larger as Pe$_s$ increases. The effects of Pe$_s$ can also be seen in the surface velocity profiles and interfacial surfactant distributions plotted in Figs. 19(a) and 19(b), respectively. The surface velocity continuously decreases, while surfactant concentration becomes less uniform as Pe$_s$ increases until about Pe$_s$=1000. After this point, Pe$_s$ does not have a signifi-
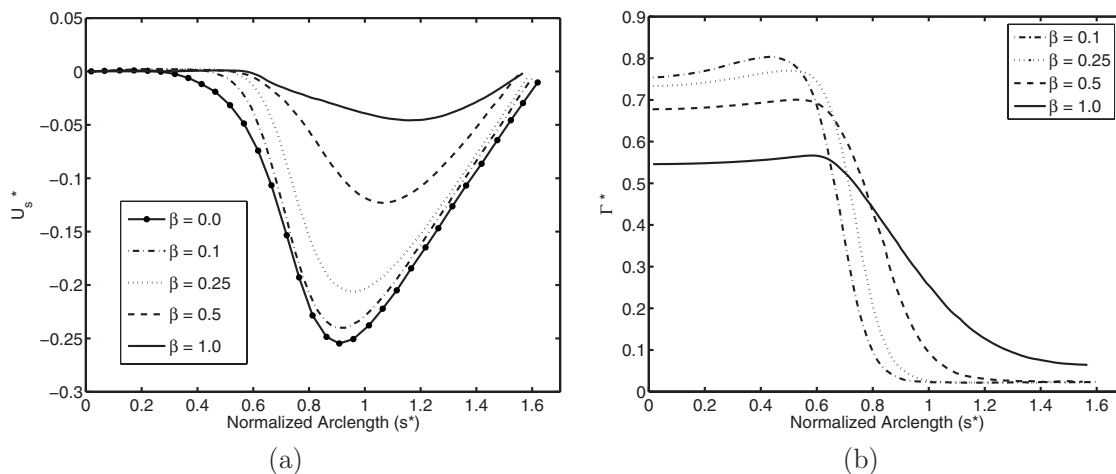

FIG. 14. Ellipsoidal bubble. (a) Surface velocity and (b) interfacial surfactant concentration as a function of nondimensional arc length measured from the centerline in the counterclockwise direction with β_s=0.1, 0.25, 0.5, and 1.0. (Eo=10, Mo=0.001, Pe$_c$=1000, Pe$_s$=100, and t^*=67.8.)
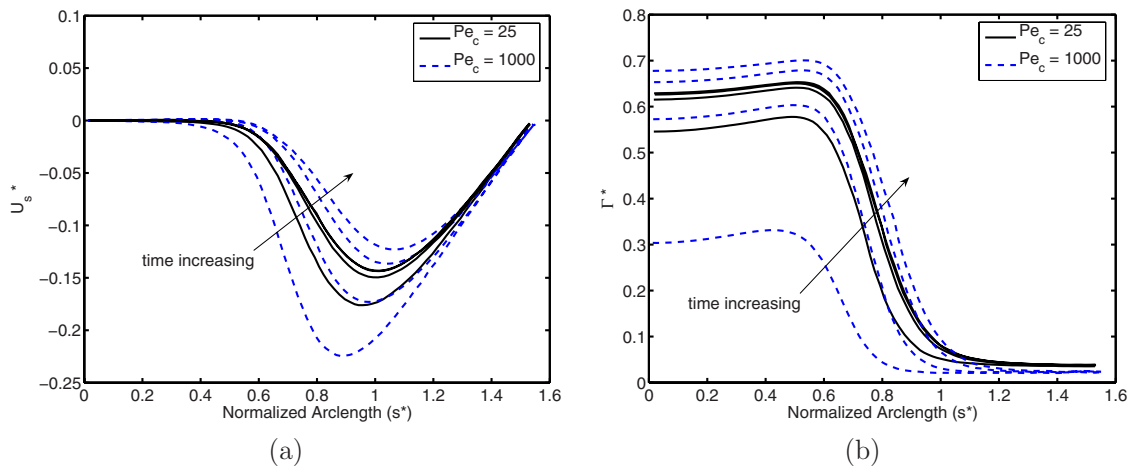
FIG. 15. (Color online) Ellipsoidal bubble. (a) Surface velocity and (b) interfacial surfactant concentration as a function of arc length measured from the centerline in the counterclockwise direction for $Pe_c=25$ (solid lines) and 1000 (dashed lines) at times $t^*=9.7$, 28.4, 48.4, and 67.8. (Eo=10, Mo=0.001, $\beta_s=0.5$, and $Pe_s=100$.)

cant influence on the surface mobility, interfacial surfactant distribution, and the bubble motion, in general.

Eötvös and Morton numbers are now set to 200 and 1000, respectively, for which a clean gas bubble takes a dimpled ellipsoidal-cap shape in an unbounded liquid in the steady motion.[1] The computations are performed both for clean and contaminated cases to show the effects of surfactants in this regime. However, a parametric study is not repeated here and a simulation is performed for a single set of parameters by setting $Pe_c=1000$, $Pe_s=100$, and $\beta_s=0.5$. The channel sizes are $D=5d$ and $L=30d$, and the computational domains of contaminated and clean cases are resolved by 256×3072 and 192×2304 uniform grids, respectively. Notice that the bubble is resolved by about 90 grid points in the axial direction for this case to better resolve the skirted rear part of the bubble. The constant contours of the bulk surfactant concentration together with the surfactant concentration distribution at the interface are plotted in Fig. 20(a), while the velocity vectors and streamlines are plotted for the con-

taminated and clean cases in Figs. 20(b) and 20(c), respectively, at $t^*=63.5$. The streamline and velocity vectors are again plotted with respect to a reference frame moving with the bubble centroid and every eighth grid points are used in the velocity vector plots. It is interesting to see that maximum interfacial surfactant concentration occurs at the back of the bubble near the centerline and there is a high surfactant concentration region in the bulk fluid in the recirculation zone. The flow field seems not to be affected much by the surfactant except that the tip of the skirted rear part is slightly sharper in the contaminated case, as can be seen in Figs. 20(b) and 20(c). The surface velocity and interfacial surfactant concentration are plotted as a function of nondimensional arc length in Figs. 21(a) and 21(b), respectively, at times $t^*=8.7$, 28.9, 46.2, and 63.5 to show the time evolution of these variables. The retardation effect of the surfactant is again seen in the surface velocity plot in this case but the effect is not as dramatic as that in the spherical bubble case.

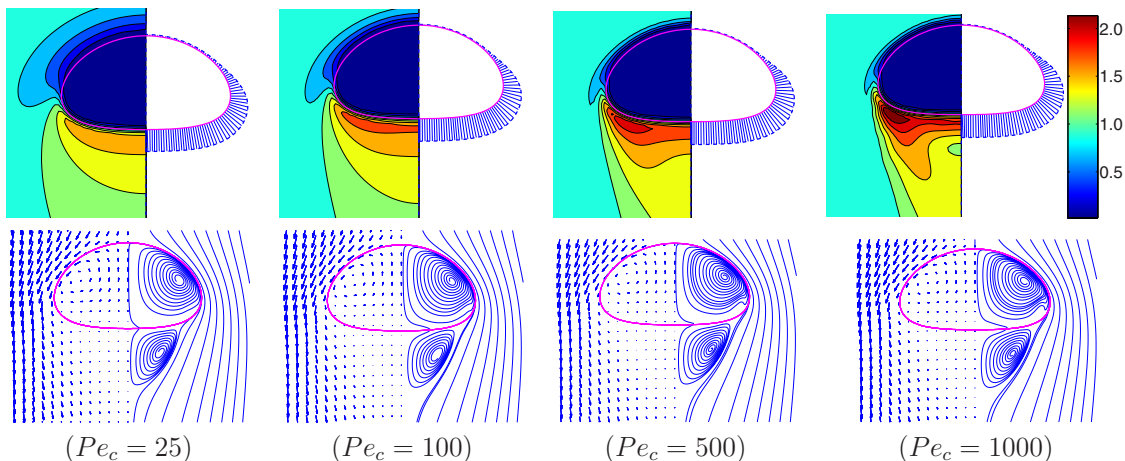(Pe_c = 25)   (Pe_c = 100)   (Pe_c = 500)   (Pe_c = 1000)

FIG. 16. (Color online) Ellipsoidal bubble. (Top row) The contour plots of the constant surfactant concentration in the bulk fluid (left side) and the distribution of the surfactant concentration at the interface (right side) with (from left to right) $Pe_c=25$, 100, 500, and 1000. (Bottom row) The velocity vectors and the streamlines in a coordinate system moving with the bubble centroid. Every third grid point is used in the vector plots. (Eo=10, Mo=0.001, $\beta_s=0.5$, $Pe_s=100$, and $t^*=67.8$.)
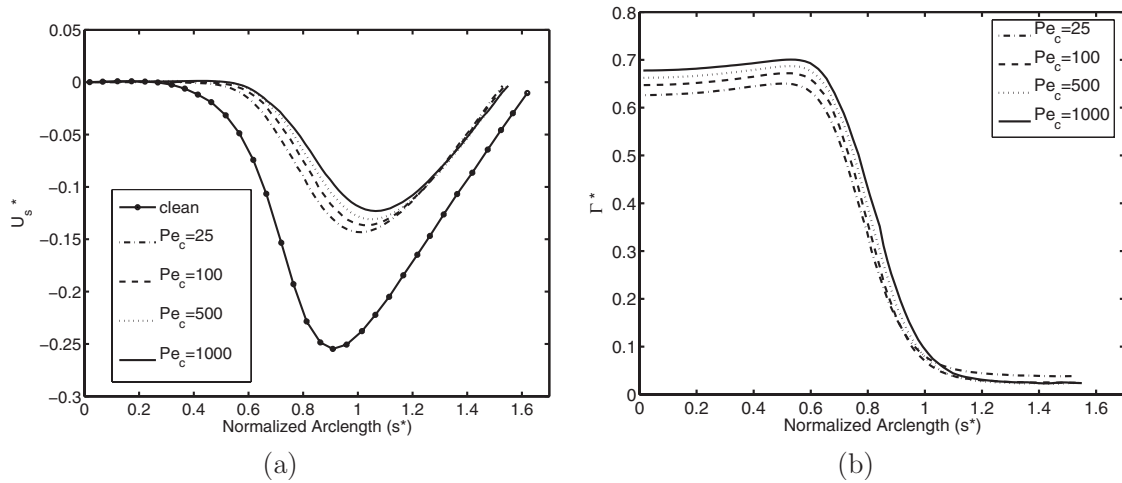
FIG. 17. Ellipsoidal bubble. (a) Surface velocity and (b) interfacial surfactant concentration as a function of arc length measured from the centerline in the counterclockwise direction for $Pe_c=25$, 100, 500, and 1000. ($Eo=10$, $Mo=0.001$, $\beta_s=0.5$, $Pe_s=100$, and $t^*=67.8$.)

The surface velocity nearly vanishes in the wake region both in the clean and contaminated cases.

Finally, the effects on the Eötvös number are studied by varying it from 0.1 to 30, while the other nondimensional parameters are kept constant at $Pe_c=100$, $Pe_s=100$, $\beta_s=1$, $D/d=15$, $L/d=30$, and $Mo=0.001$. The steady Reynolds number is plotted in Fig. 22(a) as a function of Eötvös number both for the clean and contaminated bubbles. As seen in this figure, the contamination significantly reduces the bubble terminal velocity at low Eötvös numbers, i.e., Eo <1. However, the terminal velocity of the contaminated bubble approaches that of the clean bubble for large Eötvös numbers, i.e., Eo >20. The drag coefficient is another way to examine the effects of the contamination on the terminal velocity of the bubble. For a bubble, the drag coefficient is a

function of the Reynolds, Eötvös, and Morton numbers, and it can be deduced from the balance of forces acting on the bubble. In a steady motion of a bubble, when buoyancy force balances the drag force, the drag coefficient is given by[41]

$$C_d \equiv \frac{4}{3} \frac{\Delta\rho g d}{\rho_o V_b^2} = \frac{4}{3} \frac{Eo^{3/2}}{Re^2 Mo^{1/2}}, \tag{19}$$

where V_b is the terminal velocity of the bubble. The drag coefficient is plotted in Fig. 22(b) as a function of the Reynolds number both for the clean and contaminated bubbles together with the experimental drag coefficients of fluid and solid spheres. The experimental correlations are plotted for the solid sphere when Re ≤ 100 and for the fluid sphere when
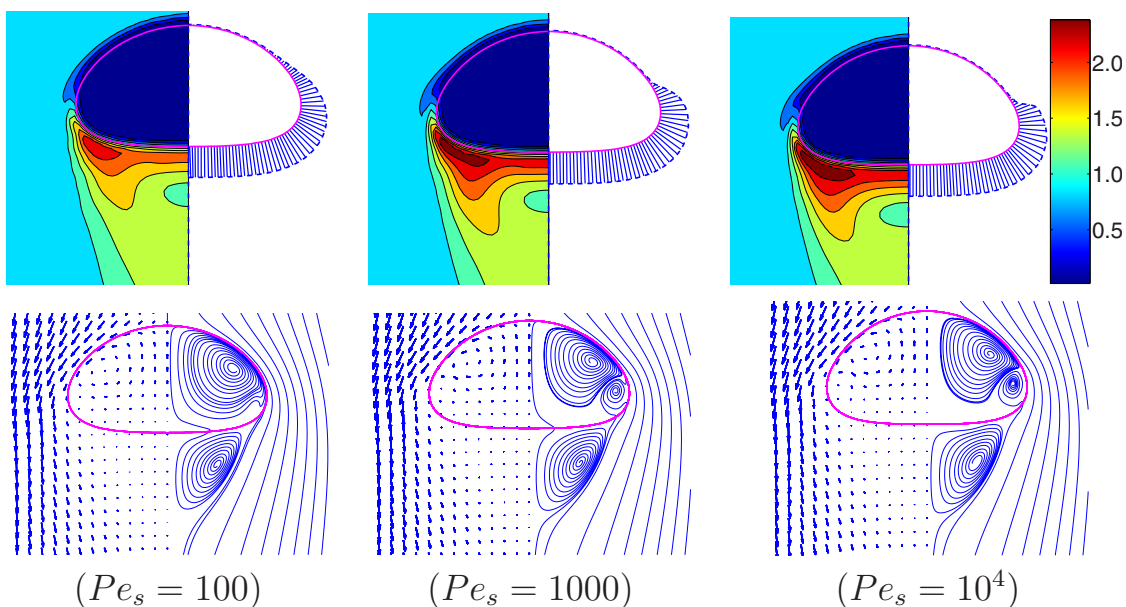

FIG. 18. (Color online) Ellipsoidal bubble. (Top row) The contour plots of the constant surfactant concentration in the bulk fluid (left side) and the distribution of the surfactant concentration at the interface (right side) with (from left to right) $Pe_s=100$, 1000, and 10^4. (Bottom row) The velocity vectors and the streamlines in a coordinate system moving with the bubble centroid. Every third grid point is used in the vector plots. ($Eo=10$, $Mo=0.001$, $Pe_c=1000$, $\beta_s=0.5$, and $t^*=67.8$.)
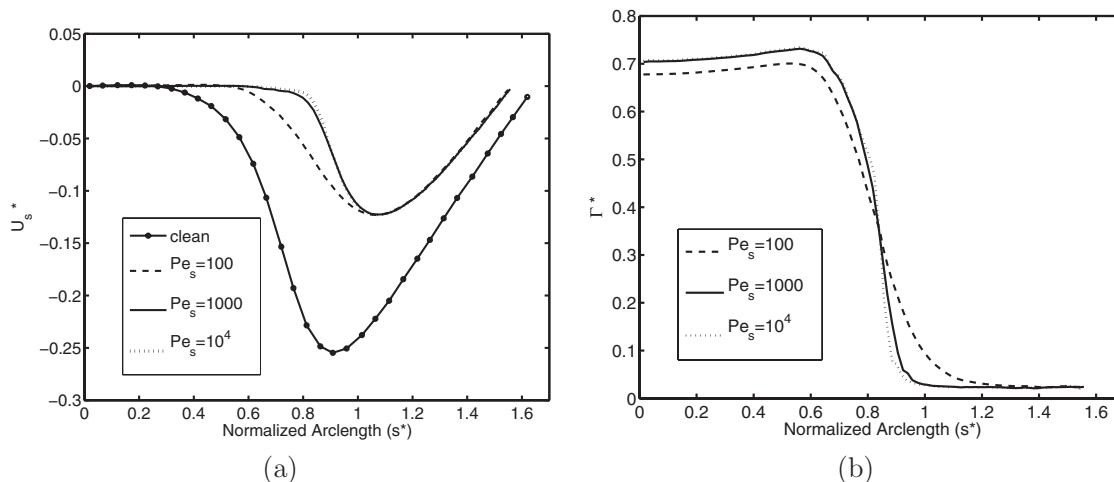
FIG. 19. Ellipsoidal bubble. (a) Surface velocity and (b) interfacial surfactant concentration as a function of arc length measured from the centerline in the counterclockwise direction for $Pe_s=100$, 1000, and 10^4. ($Eo=10$, $Mo=0.001$, $\beta_s=0.5$, $Pe_c=1000$, and $t^*=67.8$.)

$Re \leqslant 1$ as recommended by Clift *et al.*[1] As can be seen in this figure, the drag coefficient is slightly underpredicted for the clean bubble, while it is overpredicted for the contaminated bubble. We observe that the drag coefficient of the clean bubble approaches to that of the contaminated bubble at large Reynolds numbers, i.e., $Re > 30$. However, we have not observed in any case that the drag coefficient of the clean bubble exceeds that of the contaminated bubble, which is in contrast to the insoluble surfactant simulations of Jan.[41]

IV. CONCLUSIONS

The effects of soluble surfactants on the motion and deformation of a gas bubble rising in an otherwise quiescent liquid contained in an axisymmetric channel are computationally studied by using a finite-difference/front-tracking method. The Navier–Stokes equations are solved fully coupled with the bulk and interfacial surfactant concentration evolution equations, and the surface tension is related to the interfacial surfactant concentration using a nonlinear equation of state based on the Langmuir kinetics. The nearly spherical, ellipsoidal, and dimpled ellipsoidal-cap regimes are considered and effects of governing nondimensional parameters including the elasticity number, the interfacial, and bulk Peclet numbers and Eötvös number are investigated.

It is found that the surfactants generally increase the drag force and, thus, reduce the terminal velocity of the bubble. However, the retardation effect of surfactants is stronger in the nearly spherical regime than the ellipsoidal and dimpled ellipsoidal-cap regimes. In this regime, the computations are performed to study the effects of confinement on the terminal velocity of the clean and contaminated bubbles. It is found that the computational results are in very good agreement with the experimental correlations collected by Clift *et al.*[1] for the clean bubble and that the steady terminal velocity of the contaminated bubble approaches that of an equivalent solid sphere. It is also found that the surface velocity of the contaminated bubble nearly vanishes and it behaves similar to a solid sphere when it reaches a steady motion. This rigidifying effect of the surfactant is also observed in the velocity vectors and streamline plots. The effects of the elasticity number and the bulk Peclet number are also examined in this regime. It is found that both parameters have significant influence on the bubble dynamics especially during its transient motion.
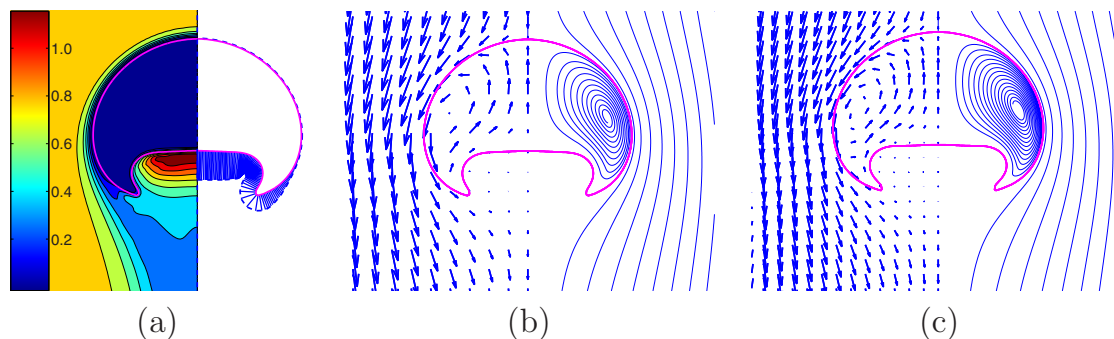

FIG. 20. (Color online) Dimpled ellipsoidal cap. (a) The contour plots of the constant surfactant concentration in the bulk fluid (left side) and the distribution of the surfactant concentration at the interface (right side). The streamlines and the velocity vectors in a frame of reference moving with the bubble centroid for (b) a contaminated and (c) a clean bubble at $t^*=63.5$. Every eighth grid point is used in the vector plots. ($Eo=200$, $Mo=1000$, $Pe_c=1000$, $Pe_s=100$, and $\beta_s=0.5$.)
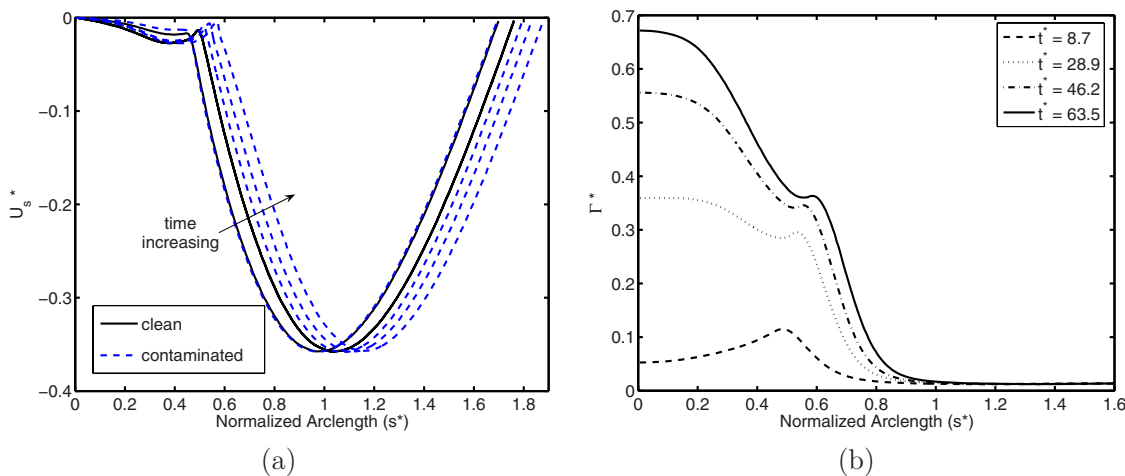
FIG. 21. (Color online) Dimpled ellipsoidal cap. (a) Surface velocity and (b) interfacial surfactant concentration as a function of arc length measured from the centerline in the counterclockwise direction at times $t*=8.7$, 28.9, 46.2, and 63.5. (Eo=200, Mo=1000, Pe$_c$=1000, Pe$_s$=100, and β_s=0.5.)

The effects of the nondimensional numbers on the bubble motion and deformation are examined more extensively in the ellipsoidal regime. It is found that β_s and Pe$_s$ generally have a profound influence on the bubble dynamics. Both parameters significantly change the surfactant concentration distribution on the interface and, thus, alter the overall flow structure. As β_s increases, the surface velocity significantly decreases, the interfacial surfactant concentration becomes more uniform, and the terminal velocity decreases. The bubble deformation first decreases with increasing β_s due to increasing rigidity of the interface, i.e., until $\beta_s < 0.5$, but it starts increasing when β_s is further increased due to overall reduction in surface tension. The flow structure is also significantly affected by β_s. A big vortex is created inside the bubble when β_s is small, i.e., $\beta_s \leqslant 0.5$ and is broken into two smaller vortices when β_s is increased beyond a critical value. In addition, the wake region behind the bubble gets larger as β_s increases. Pe$_s$ also has significant influences on the bubble motion. The interfacial surfactant concentration becomes less uniform and, similar to β_s, the big vortex

inside the bubble is broken into two smaller vortices and wake region is enlarged as Pe$_s$ is increased. We found that Pe$_c$ does not have a big influence on the bubble motion in the ellipsoidal regime in the range studied in this paper, i.e., 25 $\leqslant$ Pe$_c \leqslant$ 1000. Nevertheless the interfacial surfactant distribution slightly increases and, thus, the surface velocity is reduced as Pe$_c$ increases.

The retardation effect of the surfactant is also observed in the dimpled ellipsoidal regime but it is weaker than those in the spherical and ellipsoidal cases. The maximum interfacial surfactant concentration occurs at the back of the bubble near the axis of the symmetry. A high surfactant concentration core is created in the recirculation region in the bulk fluid and it sustains over the time due to continuous supply of surfactant released from the interface.

We also found that the drag coefficient of the clean bubble is slightly overpredicted compared to the experimental correlations, while it is underpredicted for the contaminated bubble compared to the experimental data measured for an equivalent solid sphere. In addition, it is found that the
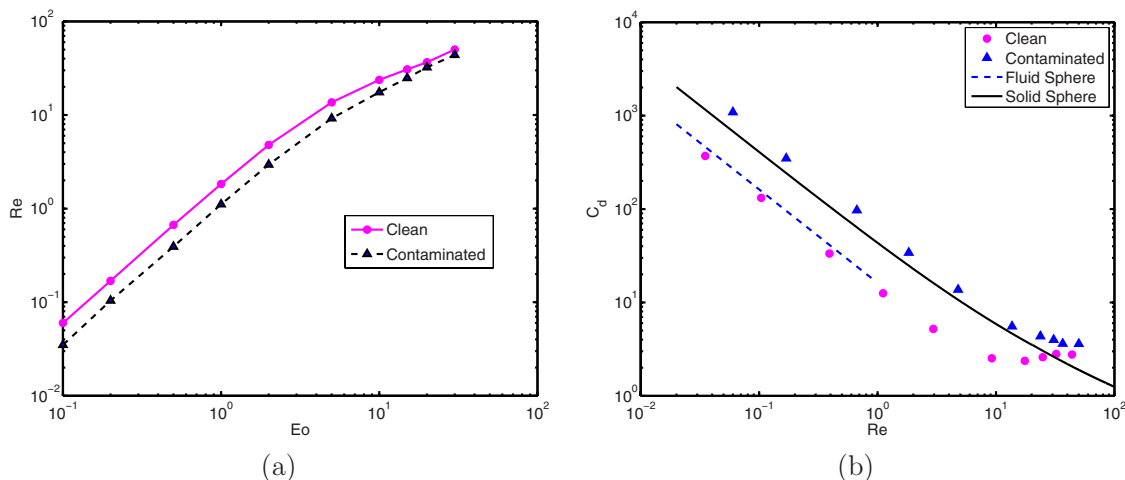

FIG. 22. (Color online) Effects of the Eötvös number on the motion of the clean and contaminated bubbles. (a) The steady Reynolds number vs the Eötvös number. (b) The drag coefficient vs the Reynolds number.

drag coefficient of a clean bubble approaches that of the contaminated bubble at large Reynolds numbers, i.e., $\mathrm{Re} > 30$.

ACKNOWLEDGMENTS

[1] R. Clift, J. R. Grace, and M. E. Weber, *Bubbles, Drops and Particles* (Dover, Mineola, 2005).

[2] H. A. Stone, "Dynamics of drop deformation and breakup in viscous fluids," Annu. Rev. Fluid Mech. **26**, 65 (1994).

[3] P. Duineveld, "The rise velocity and shape of bubbles in pure water at high Reynolds number," Ph.D. thesis, Twente University, 1994.

[4] F. Takemura and A. Yabe, "Rising speed and dissolution rate of a carbon dioxide bubble in slightly contaminated water," J. Fluid Mech. **378**, 319 (1999).

[5] J. S. Hadamard, "Mouvement permanent lent d'une sphére liquide et visqueuse dans un liquide visqueux," Compt. Rend. **152**, 1735 (1911).

[6] W. Rybczynski, "Uber die fortschreitende bewegung einer flussigen kugel in einem zaben medium," Bull. Int. Acad. Pol. Sci. Lett., Cl. Sci. Math. Nat., Ser. A **1A**, 40 (1911).

[7] A. A. Frumkin and V. G. Levich, "On surfactants and interfacial motion," Zh. Fiz. Khim. **21**, 1183 (1947).

[8] Z. He, Z. Dagan, and C. Maldarelli, "The influence of surfactant adsorption on the motion of a fluid sphere in a tube," J. Fluid Mech. **222**, 1 (1991).

[9] R. Bel Fdliha and P. Duineveld, "The effect of surfactant on the rise of a spherical bubble at high Reynolds and Peclet numbers," Phys. Fluids **8**, 310 (1996).

[10] Y. Zhang and J. A. Finch, "A note on single bubble motion in surfactant solutions," J. Fluid Mech. **429**, 63 (2001).

[11] A. Borhan and J. Pallinti, "Buoyancy-driven motion of viscous drops through cylindrical capillaries at small Reynolds numbers," Ind. Eng. Chem. Res. **34**, 2750 (1995).

[12] A. Borhan and J. Pallinti, "Breakup of drops and bubbles translating through cylindrical capillaries," Phys. Fluids **11**, 2846 (1999).

[13] E. Almatroushi and A. Borhan, "Surfactant effect on the buoyancy-driven motion of bubble and drops in a tube," Ann. N.Y. Acad. Sci. **1027**, 330 (2004).

[14] T. Yamaoto and T. Ishii, "Effect of surface active materials on the drag coefficient and shape of single large gas bubble," Chem. Eng. Sci. **42**, 1297 (1987).

[15] P. Savic, "Circulation and distortion of liquid drops falling through a viscous medium," Natl. Res. Counc. Can., Div. Mech. Eng. Technical Report No. MT-22 1953.

[16] R. Griffith, "The effect of surfactants on the terminal velocity of drops and bubbles," Chem. Eng. Sci. **17**, 1057 (1962).

[17] J. Harper, "On spherical bubbles rising steadily in dilute surfactant solutions," Q. J. Mech. Appl. Math. **27**, 87 (1974).

[18] J. Harper, "Surface activity and bubble motion," Appl. Sci. Res. **38**, 343 (1982).

[19] J. Harper, "The leading edge of an oil slick, soap film, or bubble stagnant cap in Stokes flow," J. Fluid Mech. **237**, 23 (1992).

[20] J. Harper, "Stagnant-cap bubbles with both diffusion and adsorption rate-determining," J. Fluid Mech. **521**, 115 (2004).

[21] R. Davis and A. Acrivos, "The influence of surfactants on the creeping motion of bubbles," Chem. Eng. Sci. **21**, 681 (1966).

[22] J. Holbrook and M. Levan, "The retardation of droplet motion by surfactant. Part 1. The theoretical development and asymptotic solutions," Chem. Eng. Commun. **20**, 191 (1983).

[23] J. Holbrook and M. Levan, "The retardation of droplet motion by surfactant. Part 2. Numerical solutions for exterior diffusion, surface diffusion and adsorption kinetics," Chem. Eng. Commun. **20**, 273 (1983).

[24] S. Sadhal and R. Johnson, "Stokes flow past bubbles and drops partially coated with thin films," J. Fluid Mech. **126**, 237 (1983).

[25] Z. He, C. Maldarelli, and Z. Dagan, "The size of stagnant caps of bulk soluble surfactant on the interfaces of translating fluid droplets," J. Colloid Interface Sci. **146**, 442 (1991).

[26] D. M. Leppinen, M. Renksizbulut, and R. J. Haywood, "The effects of surfactants on droplet behaviour at intermediate Reynolds numbers. I. The numerical model and steady-state results," Chem. Eng. Sci. **51**, 479 (1996).

[27] D. M. Leppinen, M. Renksizbulut, and R. J. Haywood, "The effects of surfactants on droplet behaviour at intermediate Reynolds numbers. II. Transient deformation and evaporation," Chem. Eng. Sci. **51**, 491 (1996).

[28] J. B. McLaughlin, "Numerical simulation of bubble motion in water," J. Colloid Interface Sci. **184**, 613 (1996).

[29] B. Cuenot, J. Magnaudet, and B. Spennato, "The effects of slightly soluble surfactants on the flow around a spherical bubble," J. Fluid Mech. **339**, 25 (1997).

[30] F. Takemura, "Adsorption of surfactants onto the surface of a spherical rising bubble and its effect on the terminal velocity of the bubble," Phys. Fluids **17**, 048104 (2005).

[31] Y. Wang, D. T. Papageorgiou, and C. Malderelli, "Increased mobility of a surfactant-retarded bubble at high bulk concentrations," J. Fluid Mech. **390**, 251 (1999).

[32] R. Palaparthi, D. T. Papageorgiou, and C. Malderelli, "Theory and experiments on the stagnant cap regime in the motion of spherical surfactant-laden bubbles," J. Fluid Mech. **559**, 1 (2006).

[33] K. Sugiyama, S. Takagi, and Y. Matsumoto, "Multi-scale analysis of bubbly flows," Comput. Methods Appl. Mech. Eng. **191**, 689 (2001).

[34] Y. Liao and J. B. McLaughlin, "Bubble motion in aqueous surfactant solutions," J. Colloid Interface Sci. **224**, 297 (2000).

[35] X.-J. Li and Z.-S. Mao, "The effect of surfactant on the motion of a buoyancy-driven drop at intermediate Reynolds numbers: A numerical approach," J. Colloid Interface Sci. **240**, 307 (2001).

[36] G. Ryskin and L. G. Leal, "Numerical solution of free-boundary problems in fluid mechanics. 1. The finite-difference technique," J. Fluid Mech. **148**, 1 (1984).

[37] Y. Liao, J. Wang, R. J. Nunge, and J. B. McLaughlin, "Comments on 'Bubble motion in aqueous surfactant solutions'," J. Colloid Interface Sci. **272**, 498 (2004).

[38] M. Muradoglu and G. Tryggvason, "A front-tracking method for computation of interfacial flows with soluble surfactants," J. Comput. Phys. **227**, 2238 (2008).

[39] V. G. Levich, *Physicochemical Hydrodynamics* (Prentice-Hall, Englewood Cliffs, 1962).

[40] S. O. Unverdi and G. Tryggvason, "A front-tracking method for viscous incompressible multiphase flows," J. Comput. Phys. **100**, 25 (1992).

[41] Y. J. Yan, "Computational studies of bubble dynamics," Ph.D. thesis, The University of Michigan, 1994.

[42] H. A. Stone, "A simple derivation of the time-dependent convective-diffusion equation for surfactant transport along a deforming interface," Phys. Fluids A **2**, 111 (1990).

[43] C. D. Eggleton and K. J. Stebe, "An adsorption-desorption controlled surfactant on a deforming droplet," J. Colloid Interface Sci. **208**, 68 (1998).

[44] F. H. Harlow and J. E. Welch, "Numerical calculation of time-dependent viscous incompressible flow of fluid with free surface," Phys. Fluids **8**, 2182 (1965).

[45] C. Peskin, "Numerical analysis of blood flow in the heart," J. Comput. Phys. **25**, 220 (1977).

[46] G. Tryggvason, B. Bunner, A. Esmaeeli, D. Juric, N. Al-Rawahi, W. Tauber, J. Han, S. Nas, and Y.-J. Jan, "A front-tracking method for the computations of multiphase flow," J. Comput. Phys. **169**, 708 (2001).